JOURNAL OF PROPULSION AND POWER
Vol. 10, No. 2, March–April 1994

Three-Dimensional Simulation of a Translating Strut Inlet

D. J. Singh*
Analytical Services and Materials, Inc., Hampton, Virginia 23666
Carl A. Trexler†
NASA Langley Research Center, Hampton, Virginia 23681
and
Julie A. Hudgens Young*
Analytical Services and Materials, Inc., Hampton, Virginia 23666

A three-dimensional Navier-Stokes code is used to numerically simulate the flow through a variable-geometry, reverse-sweep side wall compression scramjet inlet. The strut of the inlet is allowed to translate back and forth, it is moved forward to help start the inlet by spilling some of the air at low speed, and is moved backward once the inlet has started to provide a high contraction ratio, and therefore, high compression at high speed. The focus of this study is on detailed examination of the flow characteristics in this complex three-dimensional geometry. Flowfield features such as the top wall separation and cowl pressure, as well as the effects of reverse sweep, compression, and flow distortion (nonuniformity) are investigated. The effects of vehicle undersurface boundary-layer ingestion on the flowfield are also investigated. Comparisons with experimental results are made to provide for the assessment of the present analysis.

Nomenclature

A	=	area
AR	=	aspect ratio
CR	=	geometric contraction ratio
DI	=	distortion index
H	=	inlet height
M	=	Mach number
M_m	=	momentum-averaged Mach number
p	=	pressure
p_c	=	area-averaged compression ratio
T	=	temperature
u, v, w	=	velocities in x, y, and z directions, respectively
W	=	width of a single inlet flow passage
x, y, z	=	Cartesian coordinates
ρ	=	density

Subscript

∞	=	freestream conditions

Introduction

FOR more than two decades, NASA Langley Research Center has conducted research in development of a viable air-breathing propulsion system for hypersonic flight applications. In this flight regime, a supersonic combustion ramjet (scramjet) engine becomes attractive. The scramjet engine concept, studied extensively at NASA Langley, uses a fixed-geometry rectangular module approach that integrates well with the vehicle. On the flight vehicle, a series of rectangular scramjet modules are mounted side by side and are integrated with the airframe. The integration of the vehicle and the propulsion system takes advantage of forebody compression to reduce inlet size, and takes advantage of afterbody expansion to provide a low-drag, high-area-ratio exhaust nozzle. The basic modular concept that served as an initial focus of research in scramjet technology at Langley is shown in Fig. 1. The inlet of this module compresses the flow with the swept, wedge-shaped side walls. The sweep of these side walls, in combination with the aft placement of the cowl on the underside of the engine, allows for efficient spillage and good inlet starting characteristics over a range of operating Mach numbers with fixed geometry. Since the development of the baseline inlet concept, a number of new concepts have been developed that retain the basic features of the original design, such as fixed geometry, sweep, struts, and cutback cowl.[1]

Many of the inlet designs investigated at NASA Langley have been analyzed numerically. Most recently, a comparative study of performance parameters of a similar and a reverse sweep inlet was conducted in Ref. 2. In the similar sweep inlet, all of the compression surfaces were swept backward from the vehicle undersurface, as illustrated in Fig. 2a. The leading-edge sweep of the aft swept side walls introduces a component of velocity that is parallel to the leading edge which enhances flow spillage. In the reverse sweep inlet, alternate surfaces are swept backward and forward (Fig. 2b) to decrease the net flow downturning. This study showed some performance advantage of the reverse sweep design over the similar sweep design. The inlet with a reverse sweep had better mass capture, lower pressure increase due to the cowl, and less problem of shock wave coalescence than the similar sweep inlet. The lower cowl pressure and reduced spillage

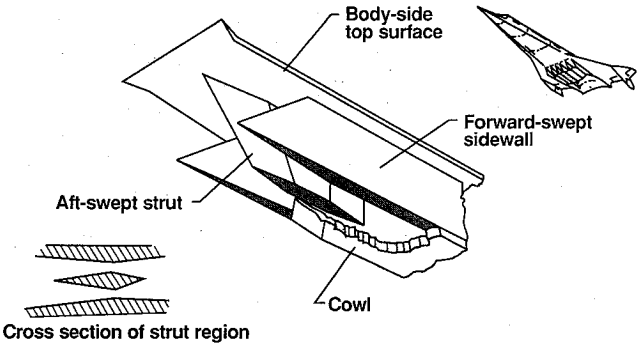

Fig. 1 Scramjet engine module and its cross section.

Received Nov. 15, 1991; presented as Paper 92-0270 at the AIAA 30th Aerospace Sciences Meeting, Reno, NV, Jan. 6–9, 1992; revision received Nov. 1, 1992; accepted for publication June 21, 1993.

*Research Scientist, 107 Research Drive. Member AIAA.
†Research Scientist, Hypersonic Propulsion Branch, Fluid Mechanics Division.

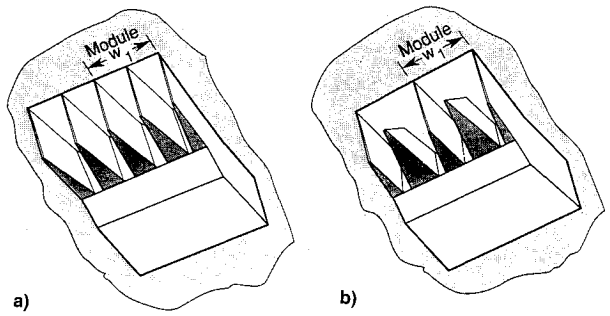

Fig. 2 Comparative configurations of a) similar and b) reverse sweep inlets.

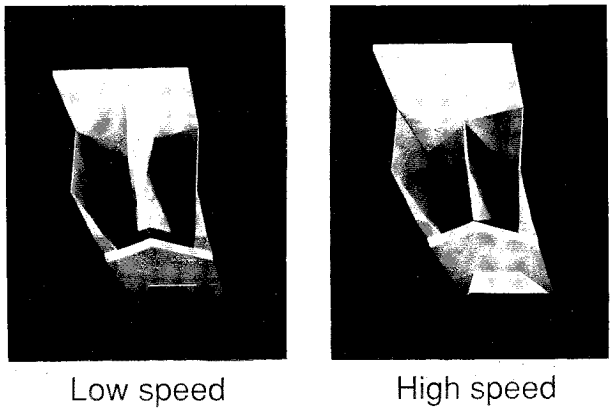

Fig. 3 Translating strut inlet concept.

result from reduced downward turning of the flow normal to the cowl plane which is caused by the forward sweep on the side walls. Also, as a result of reverse sweep, the shock waves at a given Mach number can coalesce only in certain regions (not across the entire inlet height), which alleviates the shock wave coalescence and reduces the associated boundary-layer separation problem.

Based on these results, a translating strut inlet has been designed that retains the basic features of previous designs such as the reverse sweep and cutback cowl, but also allows the strut to translate, as shown in Fig. 3. In this design, the forward placement of the translating strut relative to the fixed-cowl location permits spillage of some flow to allow inlet starting at a relatively low Mach number. Translation of the strut back and forth provides the capability to vary the contraction ratio for low-speed and high-speed operation. At low speed, the strut is moved forward, which increases the throat area (low *CR*) and permits the strut to assist inlet starting by spilling flow from the bottom of the inlet. At high speeds the strut is moved backward (high *CR*) to decrease the spillage caused by the location of the strut ahead of the cowl, which increases mass capture. Thus, for operation over a broad speed range, this variable geometry will assist inlet starting and improve high-speed mass capture.

The objective of this study is to examine the flow characteristics in this complex three-dimensional translating strut inlet. The study will concentrate on overall flow features such as pressure field, top wall separation, and cowl pressure, as well as the effects of reverse sweep and velocity field near the strut and side walls. In addition, flow distortion, momentum-averaged Mach number, and compression achieved in the throat region will also be examined. The influence of vehicle undersurface boundary-layer ingestion on the flowfield will be addressed by examining quantities such as change in the size of the separation bubble, flow distortion, and compression. Results will be shown with strut in both the forward and aft positions. The numerical results will be compared with the available experimental data to validate the computational procedure.

Inlet Geometry

The geometry of the reverse swept, side wall compression inlet model used in the present study is shown schematically in Fig. 4. The model has alternating backward and forward sweep on the compression surfaces. The solid lines show the high-speed position of the strut relative to the side walls, and the dashed lines show the strut in the low-speed position. The cowl closure begins ahead of the throat region and has a 4-deg compression. The wedge shaped strut has a 10-deg compression angle. The side walls are swept forward by 60 deg and the strut is swept backward by 50 deg. Because of the reverse sweep, the constant width throat is swept by 22 deg. The length of the inlet is 0.256 m. To simplify the implementation of numerical boundary conditions, the pointed cowl leading edge is replaced by a straight leading edge with an equal spillage area.

Numerical Method

A three-dimensional Navier-Stokes code, SCRAMIN,[3] is used to analyze the inlet configuration. The code solves the Reynolds-averaged Navier-Stokes equations in conservation form by the well-known explicit algorithm of MacCormack.[4] These equations are transformed from the physical domain to the computational domain by an algebraic coordinate transformation that generates a set of boundary-fitted curvilinear coordinates. An algebraic grid generation method is used for grid generation. The grid is clustered near the walls to better resolve both the boundary layer and the corner flow. This method is spatially and temporally second-order accurate and uses the algebraic two-layer eddy-viscosity model of Baldwin and Lomax,[5] and Sutherland's law for the molecular viscosity. The perfect gas assumption has been invoked. The calculations were conducted assuming turbulent flow on all surfaces. The code is operational on the Cray Y-MP computer at the NASA Langley Research Center.

Boundary and Initial Conditions

At the inflow boundary, the flow variables are fixed at given freestream values; at the outflow boundary, the flow variables are supersonic and are therefore extrapolated from the interior grid points. No-slip and adiabatic-wall conditions are used on the solid boundaries. The wall pressure is determined from the boundary condition that the normal derivative of pressure vanishes. On the open boundaries, extrapolation from interior grid points is used. Because the flow is symmetric about the centerline, only half of the flowfield is calculated and symmetry boundary conditions are imposed. The boundary conditions are applied in both the predictor and corrector steps. Initial conditions are normally prescribed for each set of calculations by assuming that freestream conditions exist at all grid points except at the boundaries, where proper boundary conditions are imposed. For the case that involves boundary-layer ingestion, a boundary layer is allowed to develop on a 0.3-m flat plate; this solution is then used as the inflow condition for the inlet.

Experimental Program

The facility used for the present work was the Mach 4 Blowdown Facility located at NASA Langley Research Center. The test gas is dry air supplied from the air storage system at a nominal total pressure of 1379 kPa (200 psia). The facility has a test section of 0.23 m^2 and unheated air provides a nominal Reynolds number of 68 million per meter. The model was heavily instrumented with a total of 93 static pressure orifices to determine longitudinal and lateral pressure distributions. Static pressures were obtained by electronically scanned pressure (ESP) sensors, and tunnel total pressure was obtained by one of the five analog channels. The experimental uncertainty in the pressure data was estimated to be 5%. Test times were limited to 2 min. The inlet was aligned with the flow in the flight orientation at a freestream Mach number of

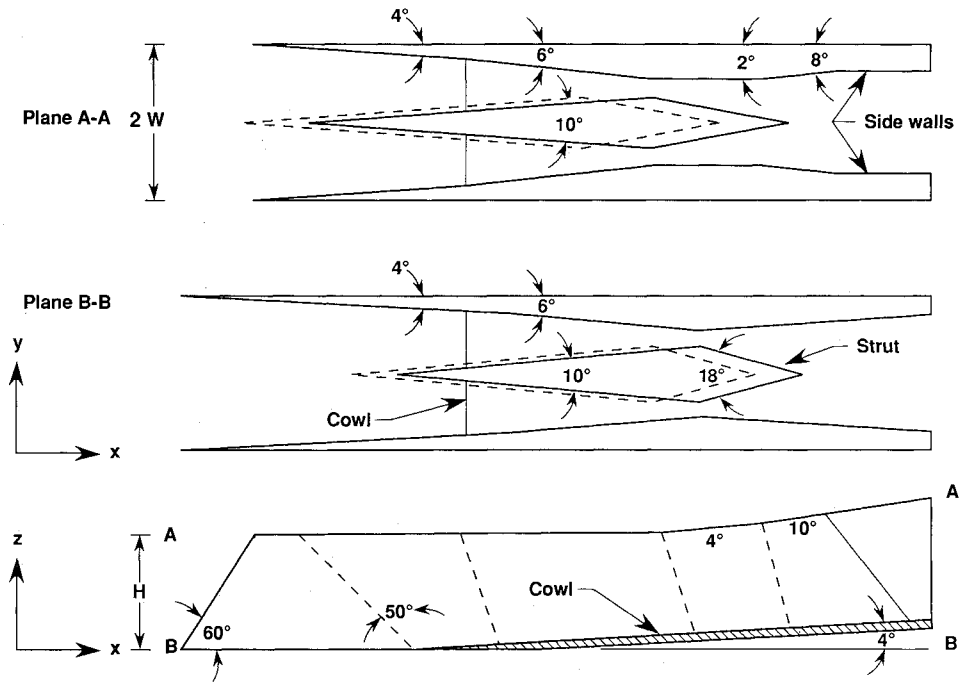

Fig. 4 Schematic of inlet geometry.

4 for all tests. A 0.3-m flat plate mounted flush with the top surface and extended ahead of the leading edge was used to generate a simulated vehicle-forebody boundary layer. The incoming boundary layer at the entrance of the inlet was approximately 10% of the inlet height.

Results and Discussion

The calculations were made at the following freestream conditions, corresponding to the experimental conditions:

$M_\infty = 4$
$T_\infty = 70$ K
$p_\infty = 8724$ N/m^2

A grid of approximately 300,000 points is used in the analysis with 93 points in the x direction, 51 points in the y direction, and 61 points in the z direction. Of the 61 points in the z direction, 17 points are located under the cowl plane to account for the end effects. These end effects arise because of the aft placement of the cowl leading edge, which leaves the inlet open to the atmosphere ahead of the cowl. Inside of the inlet, the flow that has been processed by the side wall shocks is at a higher pressure than the flow outside the inlet. This pressure differential creates an expansion wave in the cowl plane at the inlet leading edge which extends into the inlet. These end effects significantly alter the inlet flowfield, and the induced pressure gradient set up by the end effects can result in substantial flow spillage. Therefore, to account for the end effects in the numerical calculations, a portion of the external flow under the plane of the cowl was included by placing the aforementioned 17 points under the cowl plane.

The results for the strut in the forward position (low CR, case A) are discussed first, followed by results for the strut in the aft position (high CR, case B). Two sets of calculations were made for each of the two configurations. The first calculation was made with the assumption that the flow entering the inlet was uniform, and the second set simulated the ingestion of the vehicle undersurface boundary layer.

The pressure contours along three xy planes that correspond to $z/H = 0$, 0.5, and 1 are shown for case A with uniform inflow (no entering boundary layer) in Fig. 5. Although calculations have been performed for only one-half of the inlet, the results are shown for the full inlet by reflecting in the other half. This figure shows a complex system of shock waves, expansion waves, and their intersections with each other and the boundaries. The skewed shock waves that emanate from the leading edges of the wedge-shaped side walls and strut can be seen clearly. The shocks intersect with each other and return as incident shocks on the strut and side walls. The interaction of a shock with an expansion wave can be seen near the strut shoulder. The cowl shock is also visible in the $z/H = 0$ plane. Although not seen here, the intersections of the shock waves and the boundary layers cause the flow to separate near the wall, which produces small pockets of recirculating flow. The effect of the reverse sweep of the side wall and the strut is clearly evident in the figure. Because of the reverse sweep, the shock wave/boundary-layer intersection does not occur in the plane of the swept throat which reduces the blockage created by the shock-induced separation.

Figure 6 shows the pressure contours in three xz planes that correspond to $y/W = 0$, 0.5, and 1 for case A with uniform inflow. The initial contours are inclined in the $y/W = 0$ and $y/W = 1$ planes in the same direction as the sweep of strut and side wall, respectively; the contours are irregular in the $y/W = 0.5$ plane because of the combined effects of the forward and reverse sweeps. The bow shock formed by the boundary layer on the top wall and its interaction with the flowfield is clearly visible in the $y/W = 0.5$ plane. The growing displacement thickness on the top wall, in conjunction with the bow shock and the end effects, turns the flow in the downward direction. This downturned flow impinges on the cowl surface and turns parallel to the cowl surface. The impingement causes a shock to be formed, as can be seen in Fig. 6. In general, the pressure is slightly higher in the side wall plane than in the strut plane.

Figures 7a–7c show velocity vectors in three planes that correspond to $y/W = 1$, 0.5, and 0 for case A with uniform inflow. These are plotted by restricting the particle's movement to its respective plane (in the first grid plane off the wall for $y/W = 0$ and 1). The velocity vectors shown in this figure illustrate the complexity of the flowfield. The flow over most of the side wall ($y/W = 1$) and the strut ($y/W = 0$) has a downward component ahead of the cowl shock (except near the top wall) until it separates near the corner. The flow in Fig. 7b ($y/W = 0.5$ plane) is fairly uniform with a small

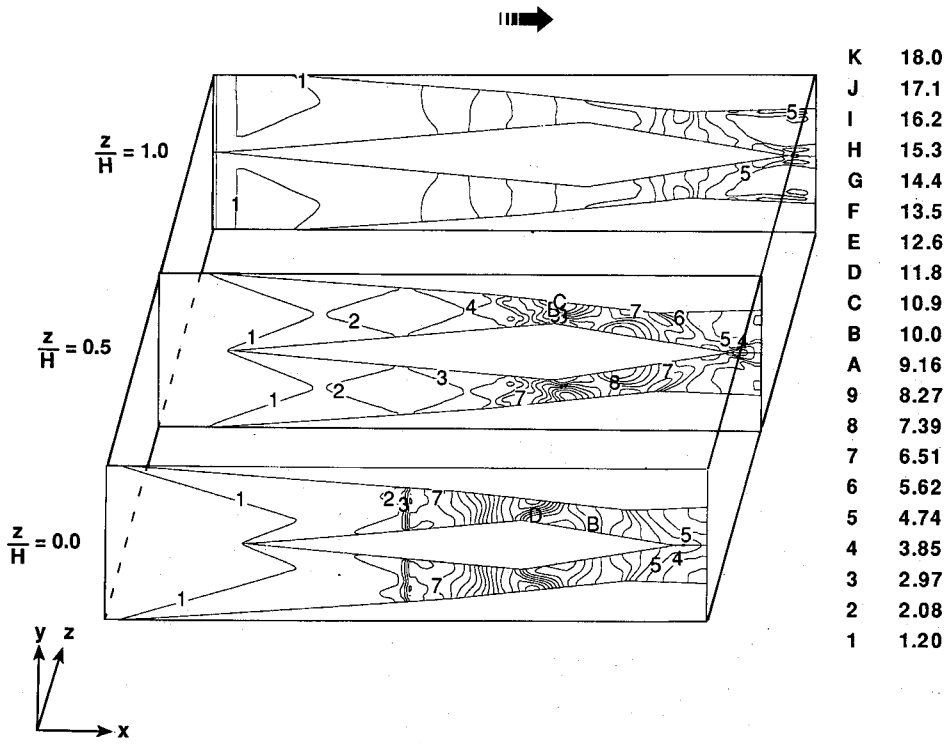

Fig. 5 Pressure contours in *xy* planes (case A with uniform inflow).

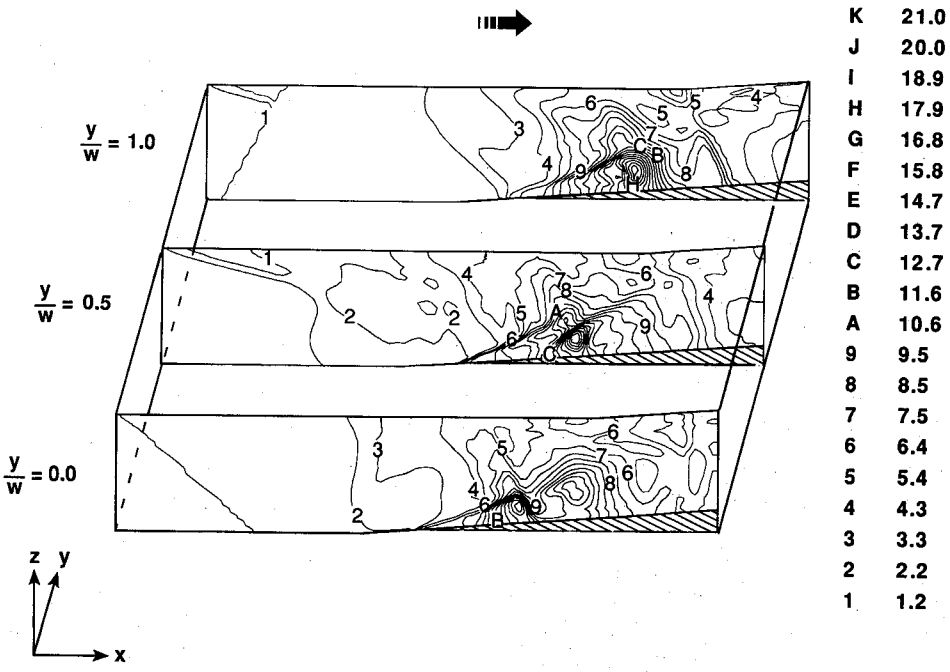

Fig. 6 Pressure contours in *xz* planes (case A with uniform inflow).

separation zone near the top wall. The size of the separation bubble is about 10% of inlet height and 15% of inlet length. The flow spillage ahead of the cowl can be seen clearly as the high-pressure flow expands into the freestream. Another interesting flow feature is the presence of a highly skewed helical velocity distribution just downstream of the cowl lip. A detailed examination of the flowfield shows that the flow near the walls lifts off as it moves toward the top wall. A similar structure was noted by Holland[6] in his investigation.

A comparison of the numerical results with the experimental data along the cowl surface and the side wall is shown in Figs. 8 and 9, respectively. The numerically predicted cowl pressure shows excellent agreement with the data. The shift near $x = 0.15$ m can be explained by the difference in the shape of the cowl leading edge between the experimental and computational model. The peak pressure is about 16 times the freestream pressure and is caused by the cowl shock. The agreement in Fig. 9 for the side wall is not as good as the comparison for the cowl pressure; the trend is captured well, but the peak pressure is overpredicted. It should be noted that the flow after $x = 0.15$ m is very complex because of the interactions of the side wall shock, the side wall expansions, the cowl shock, expansion due to end effects, and the induced shocks due to boundary-layer separation. In view of these complexities, the comparison is considered fair.

The influence of vehicle undersurface boundary-layer ingestion on the flowfield will now be examined. To simulate the incoming boundary layer, the top wall is extended by 0.3

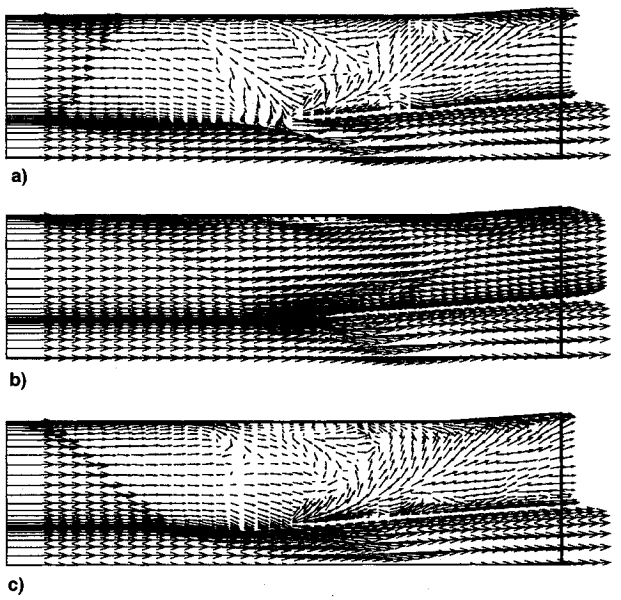

Fig. 7 Velocity vectors in xz planes (case A with uniform inflow): a) $y/W = 1.0$, b) $y/W = 0.5$, and c) $y/W = 0.0$.

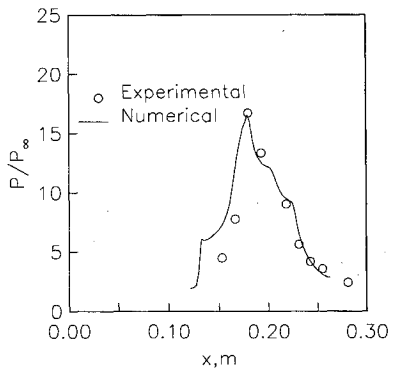

Fig. 8 Comparison of numerical and experimental results along cowl surface (case A with uniform inflow).

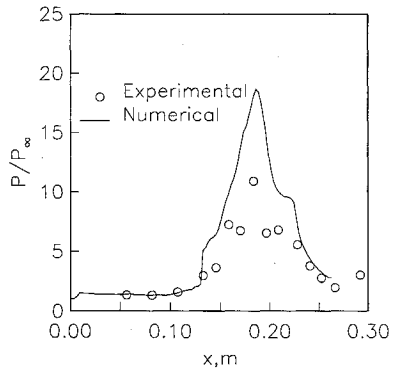

Fig. 9 Comparison of numerical and experimental results along side wall (case A with uniform inflow).

m. This generates boundary layer at the entrance of the inlet approximately 10% of the inlet height. Figures 10a–10c show the velocity vectors for case A (with boundary-layer ingestion) in three xz planes that correspond to $y/W = 1$, 0.5, and 0, respectively. The most pronounced effect is the size of the separation near the top wall which is about 15% of inlet height and 36% of inlet length. The increase in the size of separation bubble increases the pressure inside the inlet because of stronger separation shock and decreases the effective inlet area (the blockage is increased because of the bigger separation bub-

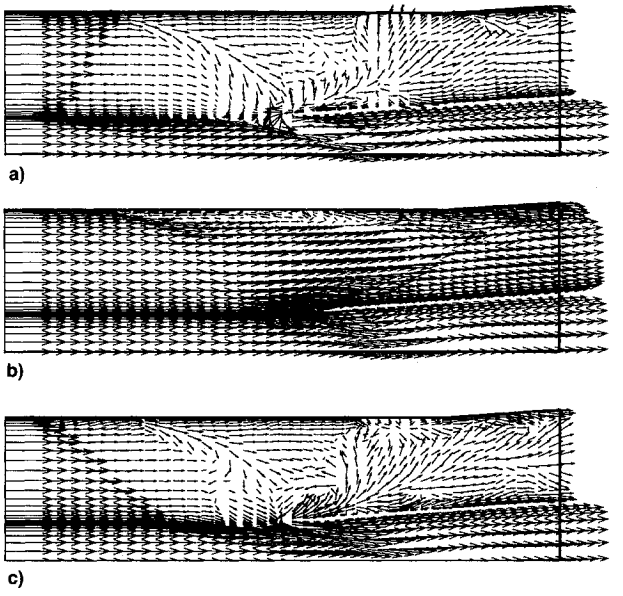

Fig. 10 Velocity vectors in xz planes (case A with entering boundary layer): a) $y/W = 1.0$, b) $y/W = 0.5$, and c) $y/W = 0.0$.

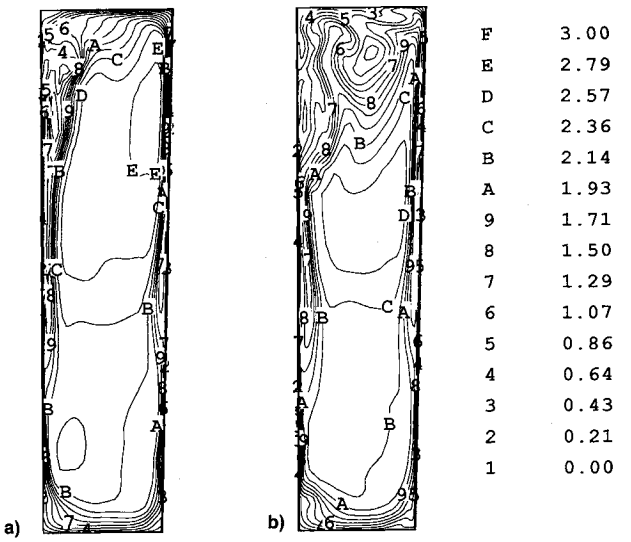

Fig. 11 Mach number contours in throat plane: a) without and b) with entering boundary layer (case A).

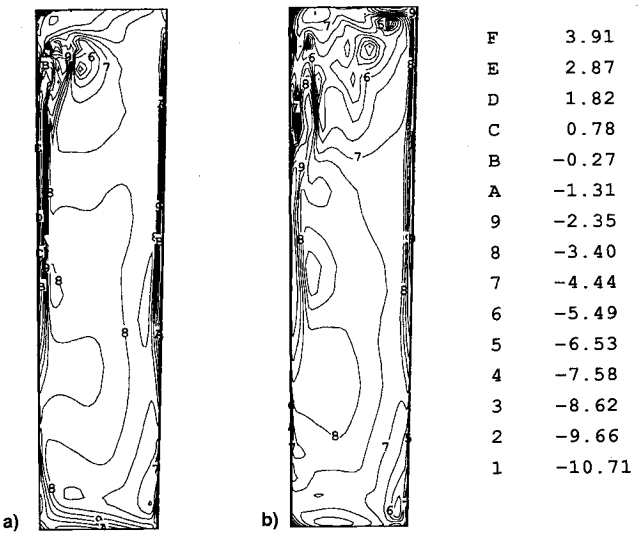

Fig. 12 Flow distortion in throat plane: a) without and b) with entering boundary layer (case A).

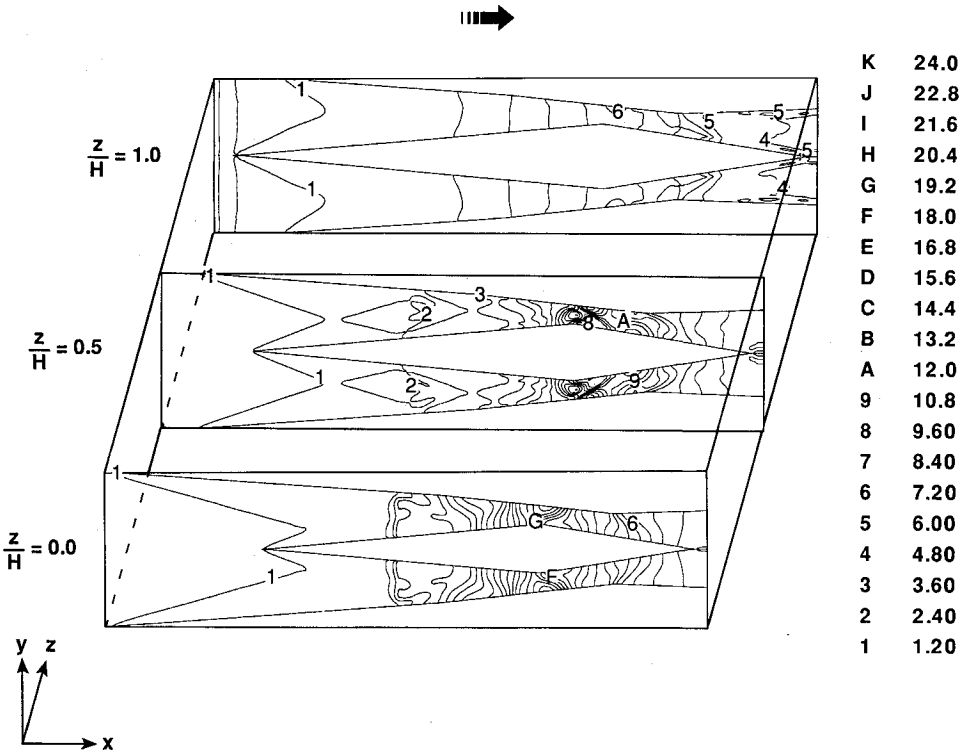

Fig. 13 Pressure contours in *xy* planes (case B with uniform inflow).

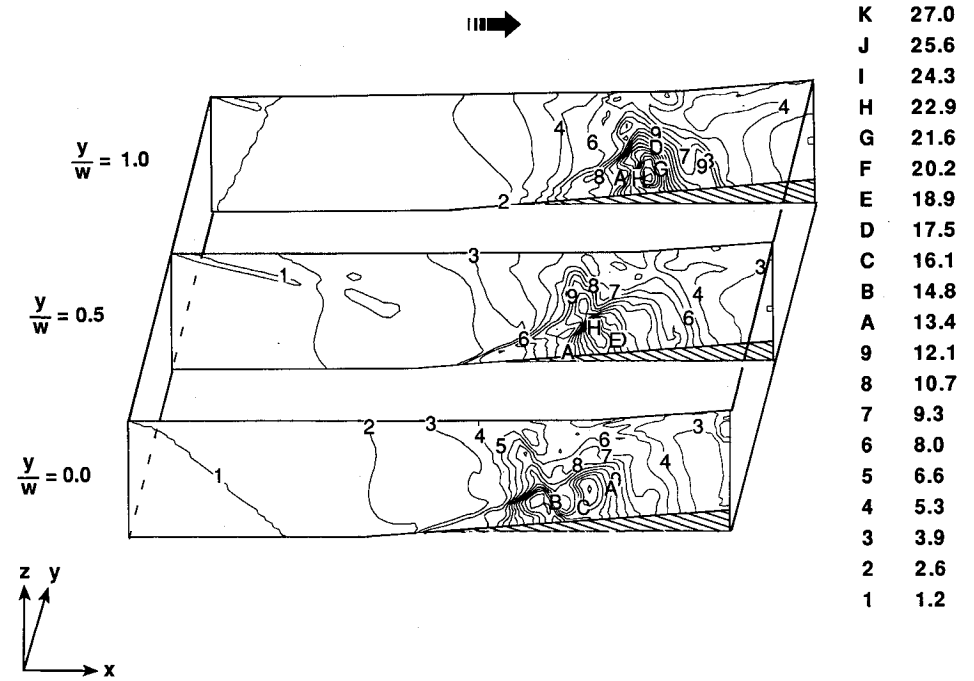

Fig. 14 Pressure contours in *xz* planes (case B with uniform inflow).

ble). Both of these effects decrease the mass capture by spilling more flow. The flow liftoff caused by the helical structure in the flowfield discussed earlier is also more clearly visible.

Figures 11a and 11b show Mach number contours in the throat plane without and with an entering boundary layer, respectively. The figure shows that two counter-rotating vortices are present near the top wall corners. A high gradient is found near the top wall, as is indicated by the concentration of contour levels. The flowfield is asymmetrical, as a result of the opposite sweep on the compression surfaces of the inlet. For the case with the entering boundary layer, a much larger region of low momentum flow exists near the top wall. Approximately 25% of the cross section is filled with the viscous nonuniform flow. This result is not surprising because the entering boundary layer near the top wall is squeezed into the throat region, which is about four times smaller in width than the entering cross section, and results in a large viscous region in the throat. In spite of the thick boundary layer, a substantial amount of good core flow exists. However, the low-energy air in the boundary layer adversely affects the inlet performance because of a flow deficit in the top portion of the inlet. In addition, it creates a larger separation region near the top wall, which generates a stronger separation shock and thus increases flow spillage.

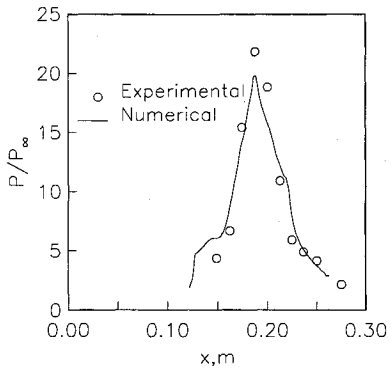

Fig. 15 Comparison of numerical and experimental results along cowl surface (case B with uniform inflow).

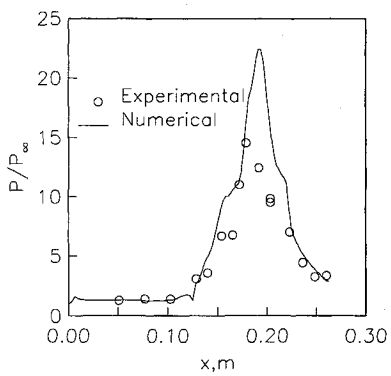

Fig. 16 Comparison of numerical and experimental results along side wall (case B with uniform inflow).

To assess the flowfield quantitatively, M_m, p_c, and DI are defined as follows:

$$M_m = \frac{\int_A \rho u^2 M \, dA}{\int_A \rho u^2 \, dA} \tag{1}$$

$$p_c = \frac{\int_A (p/p_\infty) \, dA}{\int_A dA} \tag{2}$$

$$DI = \log[(v^2 + w^2)/u^2]_{\text{throat}} \tag{3}$$

The ingestion of boundary layer reduces the M_m from 2.3 to 2.1, and increases the p_c from 9.4 to 10.5.

The parameter DI represents the ratio of transverse to streamwise velocities and is calculated at every grid point in the throat plane. For the flow with no crossflow velocity, DI will be zero. Figures 12a and 12b show the contour plot of DI in the throat plane without and with an entering boundary layer, respectively. Higher distortion can be seen in Fig. 12b as compared to Fig. 12a. The maximum distortion in both cases is near the top wall because of the presence of two counter-rotating vortices. The distortion levels in the core are almost the same; however, the core is smaller for the case with entering boundary-layer ingestion. The presence of the boundary layer therefore decreases the uniformity of airflow entering the combustor.

The results for the strut in the aft position (case B) are displayed in Figs. 13–16 (without boundary-layer ingestion). Qualitatively, the results show very similar flow features when compared to the previous case without boundary-layer ingestion. Because of the movement of the strut, the CR has increased by 18%. This increase in the contraction ratio means the entering flow is squeezed into an even smaller throat area. Figures 13 and 14 show a general increase in the pressure levels when compared to the earlier case. The comparison between the calculation and the data in Figs. 15 and 16 also shows higher peak pressures along both the cowl and the side wall when compared to the previous strut position. As in case A, the comparison is good along the cowl, but the pressure is overpredicted along the side wall. The average throat Mach number for this case is 2.1 (lower than case A), and the compression ratio at the throat is 12.9 (higher than case A).

Concluding Remarks

A numerical investigation of the flowfield in a reverse-sweep side wall compression, variable geometry inlet has been performed using a three-dimensional Navier-Stokes solver. The strut of the inlet is allowed to translate back and forth. The strut is moved forward to help start the inlet by spilling some of the air at low speed; once the inlet has started, it is moved backward to provide a high contraction ratio, and thus high compression at high speed. Flow features of the inlet at two strut positions are investigated, with emphasis on features such as top wall separation and the effects of reverse sweep and flow uniformity. Results indicate that the vehicle undersurface boundary-layer ingestion has a tendency to increase the flow separation and compression and decrease the average Mach number and overall flow uniformity. The inlet showed higher pressure along the cowl and side wall and remained started when the strut was moved backward (high CR). Numerical and experimental data are in good agreement, except in the separation zone where the calculations overpredict the pressure.

Acknowledgments

The authors would like to thank Ajay Kumar and J. P. Weidner of NASA Langley Research Center for their technical support and guidance throughout the course of this work. Thanks are also due to the reviewers for their helpful suggestions.

References

[1]Kumar, A., and Trexler, C. A., "Analysis and Projection of the Performance Prediction of Scramjet Inlets Utilizing a Three-Dimensional Navier-Stokes Code," *First Langley Symposium on Aerodynamics*, NASA CP-2397, Vol. 1, April 1985, pp. 187–208.

[2]Kumar, A., Singh, D. J., and Trexler, C. A., "A Numerical Study of the Effects of Reverse Sweep on a Scramjet Inlet Performance," *Journal of Propulsion and Power*, Vol. 8, No. 3, 1992, pp. 714–719.

[3]Kumar, A., "Numerical Simulation of Scramjet Inlet Flow Fields," NASA TP-2517, May 1986.

[4]MacCormack, R. W., "The Effect of Viscosity in Hypervelocity Impact Cratering," AIAA Paper 69-354, April–May 1969.

[5]Baldwin, B., and Lomax, H., "Thin-Layer Approximation and Algebraic Model for Separated Turbulent Flows," AIAA Paper 78-257, Jan. 1978.

[6]Holland, S. D., "A Computational and Experimental Investigation of a Three-Dimensional Hypersonic Scramjet Inlet Flow Field," Ph.D. Dissertation, North Carolina State Univ., Raleigh, NC, 1991.